scientific reports

Check for updates

OPEN

A robust nitridation technique for fabrication of disordered superconducting TiN thin films featuring phase slip events

Sachin Yadav[1,2], Vinay Kaushik[3], M. P. Saravanan[3], R. P. Aloysius[1,2], V. Ganesan[3] & Sangeeta Sahoo[1,2]✉

Disorder induced phase slip (PS) events appearing in the current voltage characteristics (IVCs) are reported for two-dimensional TiN thin films produced by a robust substrate mediated nitridation technique. Here, high temperature annealing of Ti/Si_3N_4 based metal/substrate assembly is the key to produce majority phase TiN accompanied by $TiSi_2$ & elemental Si as minority phases. The method itself introduces different level of disorder intrinsically by tuning the amount of the non-superconducting minority phases that are controlled by annealing temperature (T_a) and the film thickness. The superconducting critical temperature (T_c) strongly depends on T_a and the maximum T_c obtained from the demonstrated technique is about 4.8 K for the thickness range ~ 12 nm and above. Besides, the dynamics of IVCs get modulated by the appearance of intermediated resistive steps for decreased T_a and the steps get more prominent for reduced thickness. Further, the deviation in the temperature dependent critical current (I_c) from the Ginzburg–Landau theoretical limit varies strongly with the thickness. Finally, the T_c, intermediate resistive steps in the IVCs and the depairing current are observed to alter in a similar fashion with T_a and the thickness indicating the robustness of the synthesis process to fabricate disordered nitride-based superconductor.

Disordered superconductors have exhibited various fundamental quantum phenomena like superconductor–insulator transition (SIT)[1,2], quantum criticality[3,4], quantum phase slip (QPS)[5] etc. Of particular interest, disordered superconductors are suitable for phase slip (PS) study[5] which may lead to interesting applications in single photon detection and quantum current metrology[6]. The PS mechanism, which relates to a change in time for superconducting order parameter due to phase fluctuations, plays a crucial role for the survival of superconductivity in reduced dimension[7]. Further, the physical mechanism of dissipation in superconductors is associated with PS process[8]. For example, in 1D superconducting nanowire, the phase of the order parameter fluctuates continuously and the phase fluctuations lead to vanishing order parameter momentarily when the phase slips by 2π and thus making the wire resistive at the phase slip centers (PSCs). This is known as PS phenomenon which can be initiated by applied current for a current carrying superconductor[9].

Analogous to PSCs in 1D, phase fluctuations lead to phase slip lines (PSLs) in wide 2D superconducting films that exhibit resistive steps in current–voltage characteristics (IVCs)[10]. Experimentally PSs can be triggered by magnetic doping[11,12], embedding artificial pinning centers[13] or by using magnetic field[7]. Here, we address the effects of disorder on the dynamics of IVCs for quasi 2D TiN thin films. In recent years, ultrathin TiN films have been reported to exhibit SIT[14], quantum criticality[14] and Berezinskii–Kosterlitz–Thouless (BKT) transition[15]. Further, it has been reported that disordered TiN can be a promising candidate for QPS study[16,17]. Here, we report the formation of PSLs by observation of staircase-like structures appearing in the IVCs for disordered TiN thin films. We demonstrate that by tuning the disorder the superconducting-to-normal state transition in the measured IVCs changes from a single step transition to a transition embedded with multiple steps featuring the formation of PSLs. The tuning of disorder level in TiN films has been achieved by adopting a novel substrate mediated nitridation technique[18–20], which employs high temperature annealing of Ti/Si_3N_4 based metal/

[1]Academy of Scientific and Innovative Research (AcSIR), AcSIR Headquarters CSIR-HRDC Campus, Ghaziabad, Uttar Pradesh 201002, India. [2]Electrical & Electronics Metrology Division, National Physical Laboratory, Council of Scientific and Industrial Research, Dr. K. S Krishnan Road, New Delhi 110012, India. [3]Low Temperature Laboratory, UGC-DAE Consortium for Scientific Research, University Campus, Khandwa Road, Indore 452001, India. ✉email: sahoos@nplindia.org

substrate assembly to prepare majority phase TiN thin films accompanied by $TiSi_2$ and elemental Si as minority phases[18]. Conventionally, TiN films are grown either by using reactive dc sputtering of Ti in presence of Ar/N_2 gas mixtures[21–26] or by atomic layer deposition[27,28] in presence of N_2 gas etc[29–31]. However, a fine tuning of nitrogen concentration is needed to achieve the stoichiometric highly crystalline fcc TiN known to possess higher superconducting critical temperature (T_c).

By using this substrate mediated nitridation technique, we have produced 3–20 nm thick TiN films with T_c ranging from 3.0 to 4.8 K, respectively, and the results are comparable to the best reported values[21,27,29]. Here, we address the effects of T_a and film thickness on the superconducting properties of TiN thin films. The maximum T_c obtained is around 4.8 K for the film with thickness 20 nm and annealed at 820 °C. T_c decreases with the decrease in T_a & film thickness. Further, the formation of PSLs and their evolution in the IVCs have been studied under the application of external fields. Finally, we have investigated the effects of T_a and film thickness on the temperature dependent critical current (I_c) by using Ginzburg–Landau (GL) theory[32] and we have found that the I_c and the PSLs vary in a similar fashion with T_a and the film thickness.

Results and discussion

The temperature dependent resistance [$R(T)$] measurements on thin films-based samples are presented in Fig. 1. The device configuration in conventional four probe measurement scheme for a representative sample is shown in the inset of Fig. 1a. The width of the film is around 500 μm and the distance between the two voltage leads is around 1.1 mm. A set of zero field $R(T)$, measured on the batch of 12 nm thick samples annealed at different T_a, is presented in Fig. 1a. During the course of $R(T)$ measurements from room temperature to 2 K, the samples undergo normal (NM) to superconducting (SC) phase transition which strongly depends on T_a. It is evident from Fig. 1a that the NM-SC transition shifts towards lower temperature for lower values of T_a. For example, the highest T_c appears for $T_a = 820$ °C, whereas, we do not observe any transition down to 2 K for the sample annealed at 650 °C. The various critical temperatures are defined in Fig. 1b which displays the thickness dependent $R(T)$ data for samples annealed at 820 °C. Here, the film thickness varies from 20 to 3 nm. The T_c is defined as the temperature at which the derivative dR/dT becomes maximum, which is shown by the dashed vertical line in Fig. 1b for the representative sample of thickness 3 nm. The maximum T_c of about 4.8 K is obtained for the sample TN1 of 20 nm thickness. With thickness decreasing from 20 to 12 nm as that for sample TN2, the T_c is reduced to 4.76 K indicating a very little change or saturation in T_c for the films with thickness ≥ 12 nm. With further reduction in the film thickness, T_c reduces from that of the maximum T_c of TN1 (~ 20 nm) by 0.4 K, 1.2 K and 1.8 K for samples TN3 (~ 8 nm), TN4 (~ 4 nm) and TN5 (~ 3 nm), respectively. This implies that the effect of film thickness on T_c becomes prominent for the thickness around 10 nm and below. The reduction in film thickness increases the normal state resistance (R_n). Intially, the change in R_n from 20 nm (27.6 Ω) to 12 nm (86.8 Ω) is more than 3 times. With further decreasing thickness, R_n increases to more than 5.5 times for 8 nm (154 Ω), 11.8 times for 4 nm (327 Ω) and 27.8 times for 3 nm (769 Ω) with respect to 20 nm thick sample. However, the change in R_n with respect to T_a, as shown in Fig. 1a, is apparently random and will be discussed later.

Further, we have collected the T_c^{Onset} and T_c^{Zero} values for samples with various thickness for T_a equal to 820 °C, 780 °C and 750 °C and those are displayed with respect to thickness in Fig. 1c. For $T_a = 820$ °C and 780 °C, T_c strongly depends on thickness in the lower thickness regime (thickness ~ 4 nm and lower), whereas, for $T_a = 750$ °C, the variation in the T_c with thickness is very little and the same is marked by the dotted circle. The overall variation of the T_c on T_a and film thickness is displayed by color plot in Fig. 1d which is divided into several zones. Based on the increasing order of the T_c, the regimes I-to-IV are separated from each other. Regime-I, the lowest T_c regime, corresponds to a very little change of about 0.1 K in T_c with thickness in the range of 4 nm and below for $T_a < 780$ °C. In comparison with regime-I, regime-II is noticeably different. Here, for $T_a > 780$ °C, T_c remains almost unchanged for a very narrow thickness range, whereas, for $T_a < 780$ °C, a wide span of thickness delivers almost the same T_c. Hence in regime-II, the T_c shows strong dependence on thickness for higher T_a. In regime-III, the effect of increased T_a or increased thickness results in same direction towards increasing T_c. Finally, the highest T_c zone regime-IV is originated mainly from higher T_a (≥ 780 °C) and here, the T_c is observed to saturate for increased thickness. However, for the case of higher film thickness (~ 4 nm and above), the T_c strongly varies with T_a from 3.12 to 4.76 K. Therefore, T_a plays a significant role in changing the T_c ranging from 4.76 K for 820 °C to no transition down to 2 K for 650 °C for 12 nm thick films. Apart from the T_c, the influence of T_a is also observed on R_n as already evident in Fig. 1a. Here, R_n reduces with decreasing T_a from 820 to 750 °C and further reduction in T_a leads to increased R_n. Unlike T_c, the dependence of R_n on T_a is not straightforward and that is mainly due to the presence of minority phases like $TiSi_2$ and Si that are generated and modulated by the annealing process[18]. Here, R_n varies in the range between 60–87 Ω for T_a ranging from 820 to 700 °C with its maximum value of about 87 Ω occuring at $T_a = 820$ °C. In order to have a clear understanding of the anomaly in R_n variation with T_a, we have displayed X-ray photoelectron spectroscopy (XPS) core-level binding energy spectra for Ti 2p, N 1s and Si 2p from the reference samples in Fig. 2a–c, respectively. These reference samples were fabricated simultaneously with the batch of samples shown in the Fig. 1a. Ti 2p and N 1s spectra clearly indicate the presence of TiN as the dominant phase for almost all the studied T_a, whereas, there is a striking difference in Si 2p spectra presented in Fig. 2c which indicates a clear shifting from the $TiSi_2$ phase towards elemental Si for $T_a > 780$ °C. As the resistivity of $TiSi_2$[33] is lower than that of TiN[34] and of Si, the reduced R_n for $T_a \leq 780$ °C compared to that of $T_a = 820$ °C can be originated from the amount of $TiSi_2$ present in the composite film. Further, the relative concentration of minority $TiSi_2$ phase changes with T_a[18] and hence, R_n is expected to change with T_a. As evident from Fig. 2c at $T_a = 820$ °C, a majority of the decomposed Si from Si_3N_4 substrate remains as elemental Si which in turn contribute to the increased resistance in the normal state[18]. However, the change in R_n with respect to thickness [Fig. 1b] is much more than the change due to the variations

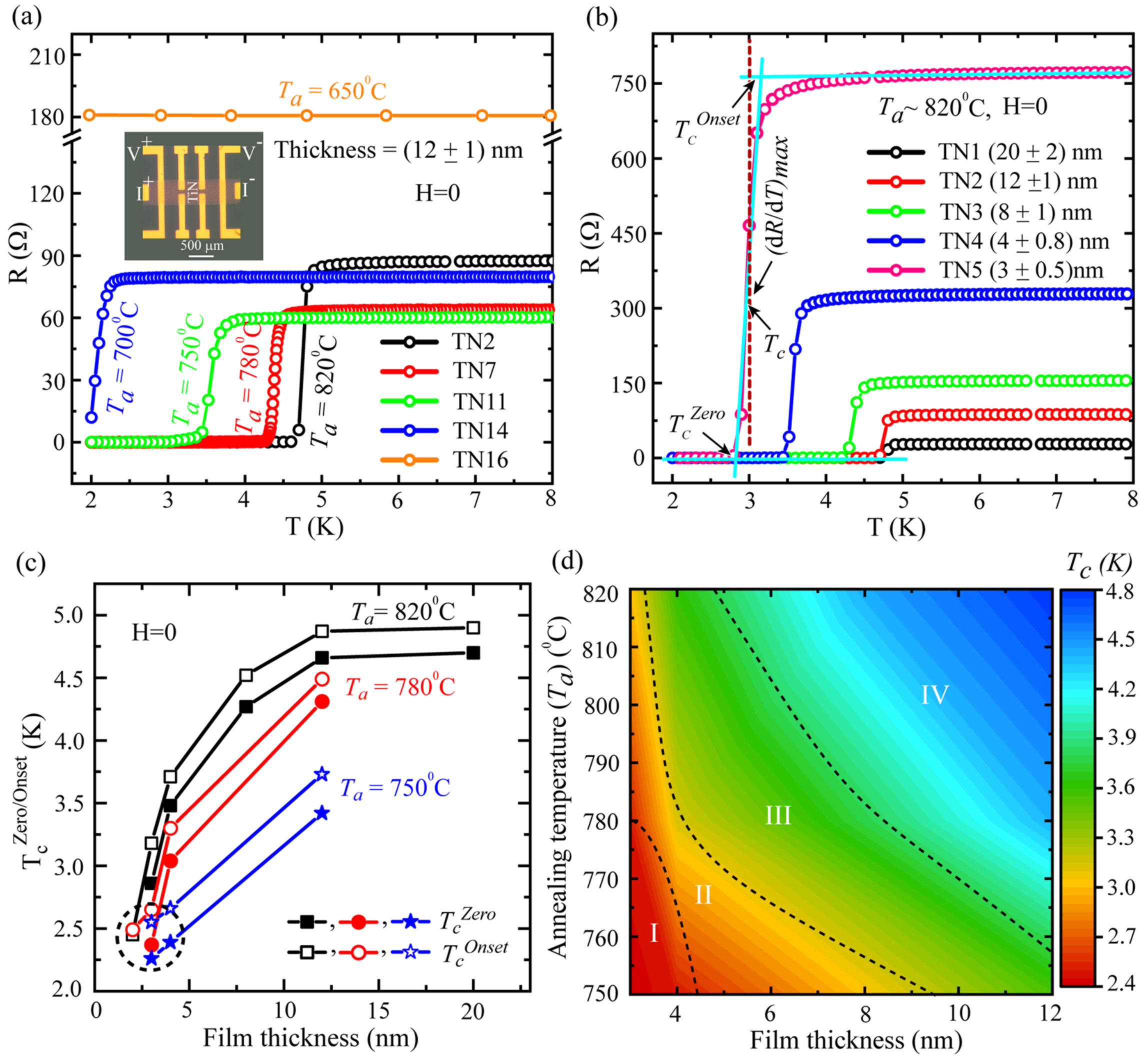

Figure 1. Superconducting properties probed by temperature dependent resistance $R(T)$ measurements. (**a**) A set of $R(T)$ measurements done on TiN thin films grown at varying annealing temperature (T_a) while keeping the thickness same of about 12 nm. Inset: Optical microscopy image of a representative multiterminal device showing the measurement scheme for tranport measurements in four probe geometry. (**b**) A different set of $R(T)$ measured on samples with varying thickness but annealed at same temperature, T_a = 820 °C. Different critical temperatures, (T_c^{Onset}, T_c^{Zero} and T_c), are defined as shown in (**b**) for the representative curve with thickness around 3 nm. (**c**) Thickness dependent T_c values collected from the samples annealed at T_a = 820 °C, 780 °C and 750 °C. (**d**) A contour color plot representation of the summary related to the dependence of critical temperature (T_c) on thickness and annealing temperature (T_a). Different regions are marked by Roman numerals and are bounded by the dashed boundary lines.

in T_a [Fig. 1a]. For comparison, we have presented R_n with respect to T_a and thickness by using 3-D color plots in Fig. 2d. It is apparent that R_n is mainly dominated by the thickness variations.

Finally, from Figs. 1, 2, we have demonstrated the variation of T_c & R_n with thickness & T_a for disordered TiN thin films accompanied by nonsuperconducting minority phases of $TiSi_2$ and Si[18]. As T_a plays a huge role in the decomposition of Si_3N_4 and diffusion of Si & N elements inside the film[18], the influential role of T_a on particularly the superconducting properties of TiN thin films is also confirmed by the present study. It is noteworthy to mention that the achieved best T_c by employing the current synthesis technique can be comparable, and some cases can be even better than, the reported conventional methods [Table S1 in the Supplementary Information (SI)].

So far, we have discussed the influence of film thickness & T_a on T_c and R_n. Now, we consider the effect of film thickness and T_a on the IVCs for samples prepared under different growth conditions. In Fig. 3, we display IVCs of three selective samples, namely, TN4, TN8 & TN12, that are annealed at 820 °C, 780 °C & 750 °C, respectively. Each of these selected samples are of 4 nm thickness which is less than their respective coherence length ξ(0) [Fig. S5 in SI]. This indicates that the samples are in the 2D limit, where phase fluctuations lead to PSLs[35] and *IVCs* exhibit resistive steps[20,36,37]. In Fig. 3a, we display a set of zero field $R(T)$ measured on the aforementioned three representative samples. Similar to Fig. 1a, here also we observe a shifting of the NM-SC phase transition towards lower temperature for reduced T_a. For example, T_c changes from 3.6 K for sample TN4 (~820 °C) to

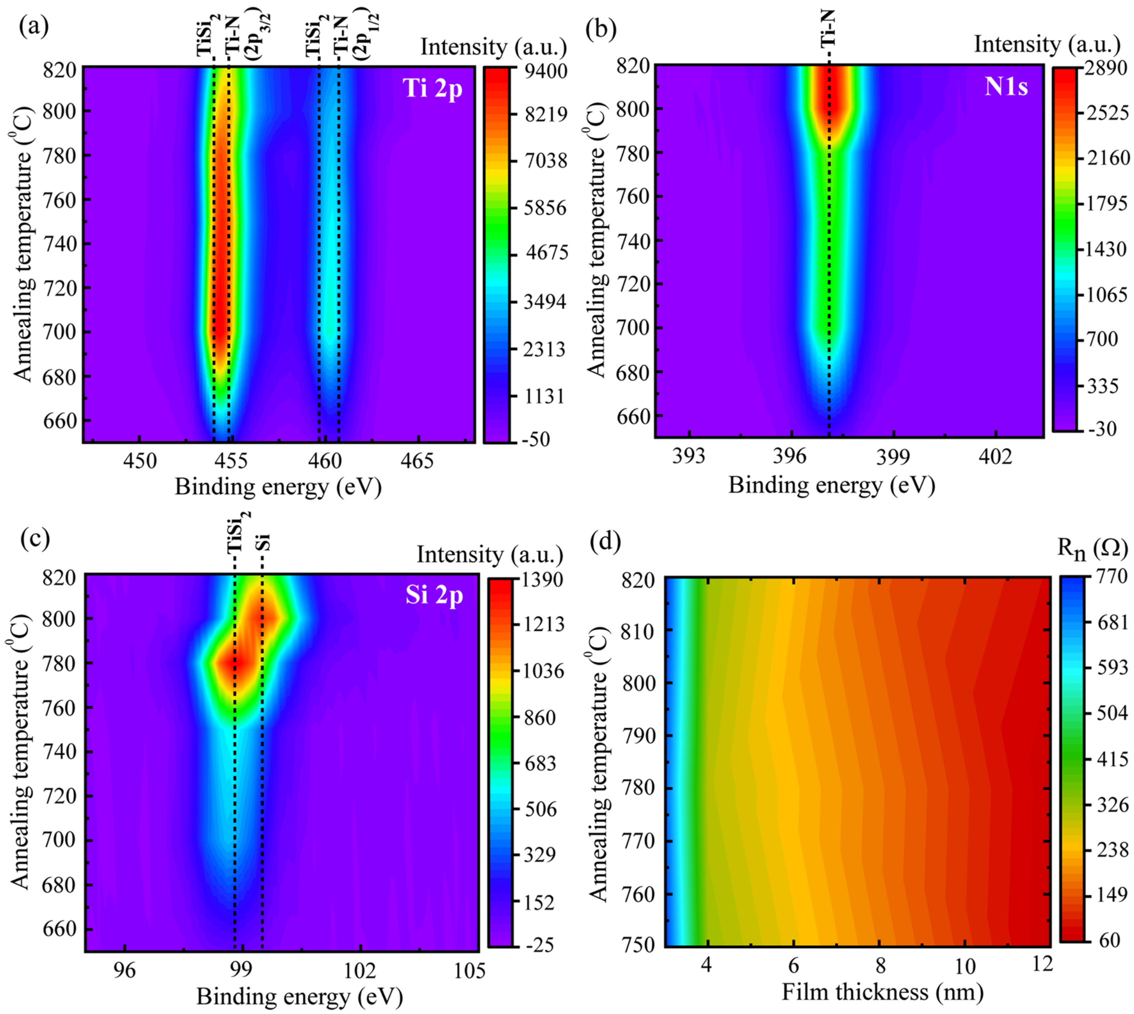

Figure 2. Core-level XPS binding energy spectra of (**a**) Ti 2p, (**b**) N 1 s and (**c**) Si 2p for reference samples annealed with varying annealing temperatures. The XPS spectra were taken from inside the films after removing the top surface by Ar^+ ion sputtering at 500 eV for about 2 min. (**d**) Variation in the R_n with the variations in T_a and thickness of the films.

3.12 K for sample TN8 (~ 780 °C) to 2.5 K for sample TN12 (~ 750 °C). However, very little variation in R_n is observed among the samples. First, we present the IVC isotherms for sample TN4 in Fig. 3b which shows a single step sharp switching during the phase transition from the superconducting-to-metallic state at temperature far below the T_c. The current at which the switching occurs is known as the critical current (I_c), whereas, the current corresponding to the onset of superconducting state from the normal state during the downward sweeping direction is defined as the retrapping current (I_r) [Fig. S6 in SI]. For all the measured samples, these two characteristic currents are different and the IVCs appear to be hysteretic with respect to the current sweeping direction. With increasing temperature, the hysteresis reduces and finally vanishes at T_c as shown in Fig. S6 in SI. Hysteretic IVCs are commonly observed in granular superconducting films due to the Joule heating effect, which locally increases the effective temperature and hence reduces the I_c[38,39]. Further, at temperatures close to the T_c, intermediate resistive steps start to appear at 3.0 K and higher temperature as highlighted by the red dotted arrows in Fig. 3b. The slopes of these resistive states increase in the increasing current direction and they converge at one single point [the grey dotted lines], known as the excess current I_s. These characteristics indicate that the intermediate resistive states originate due to PSLs[8,11]. Besides, the intermediate resistive steps become more prominent for the sample TN8 as shown in Fig. 3c. A single sharp switching is observed at 2.4 K and below but the sudden emergence of intermediate resistive steps takes place for the isotherms measured at 2.5–2.8 K. Further, black dotted lines connecting the slopes of each resistive steps meet at a single point on the current axis at I_s confirming the formation of PSLs in disordered TiN thin films. These intermediate resistive steps get more prominent even at lower temperature for the sample TN12 as shown in Fig. 3d. Here, the resistive states exist for much wider extent in current indicating the reduced T_a indeed play a favorable role in support of PSL formation.

Reduction in thickness introduces more disorder[14,40–42] as that is also evident in the increased R_n presented in Figs. 1b and 2d. However, relating disorder directly to the resistivity would not be appropriate in the present scenario as there are secondary phases present along with TiN. Here, the disorder is related mainly to the granularity and the grain size of the films as the surface morphology studied by SEM and AFM [Fig. S1-S3 in the SI] suggests

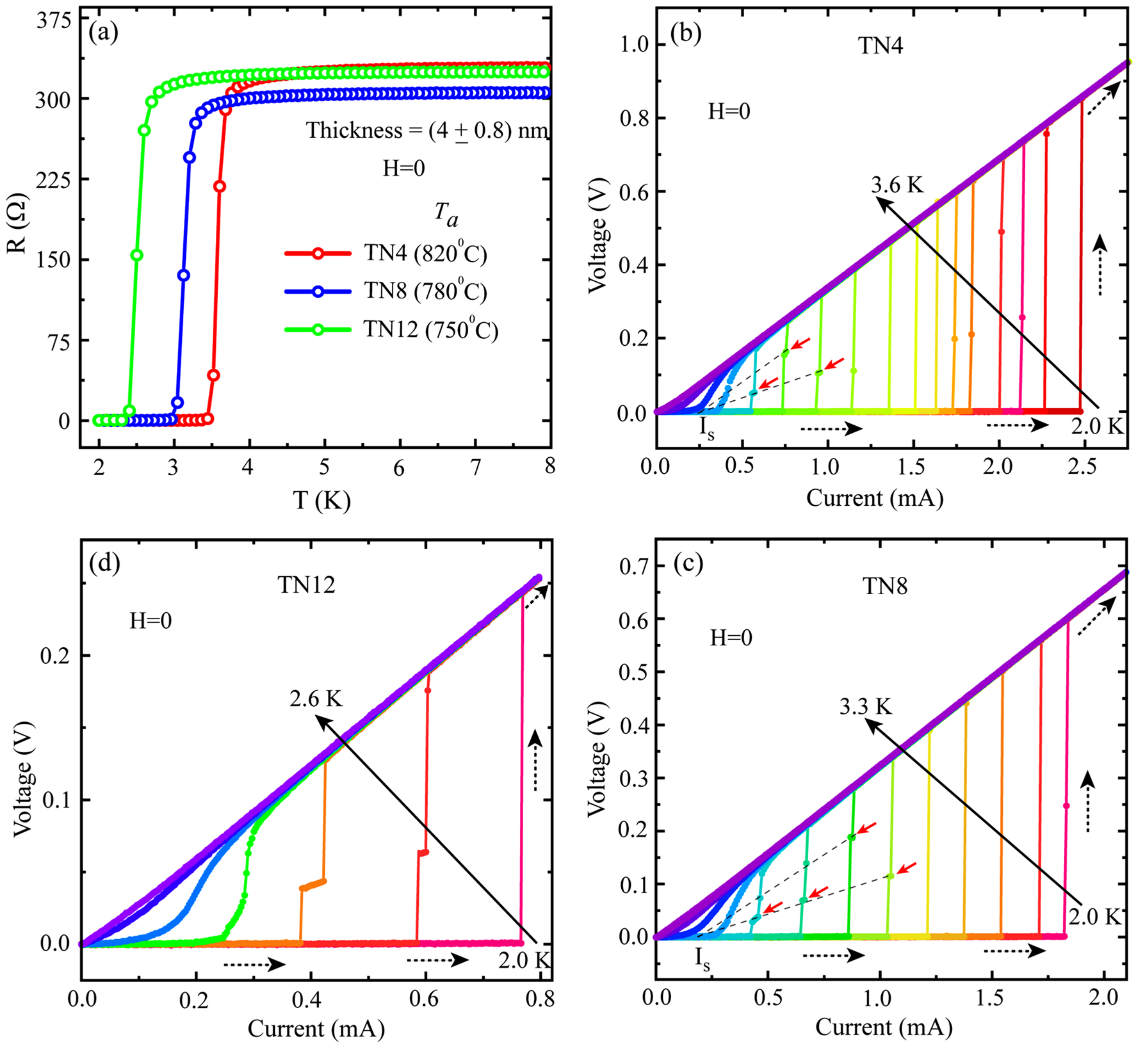

Figure 3. Zero-field current–voltage characteristics (IVCs). (**a**) Collection of *R(T)* data measured on three selected samples for which the IVCs are displayed in (**b**–**d**). The three representative samples (TN4, TN8 & TN12) are of same thickness (~ 5 nm) but were grown at different annealing temperatures. The IVC isotherms for (**b**) TN4 (T_a = 820 °C), (**c**) TN8 (T_a = 780 °C) and (**d**) TN12 (T_a = 750 °C). The black dashed arrows indicate the sweeping direction of the bias current along with the transition from superconducting to normal state. The solid black arrows specify the extent in measurement temperature starting from the base temperature (2.0 K) up to the T_c with 0.1 K interval. Here, only the upward direction of current sweeping is considered while presenting the IVCs. The red arrows show the appearance of intermediate resistive states.

the variations in the grain size with sample thickness. Generally, granular superconductors can be considered as an array of Josephson junctions where superconducting grains act as the superconducting islands and the grain boundaries serve as the weak-links and the macroscopic superconductivity is established by superconducting proximity effect. However, the establishment of macroscopic coherence depends strongly on the grain size and the inter-granular distance. Further, the intergranular region is very important as it contributes to the disorder by possessing any impurity like the presence of Si and the silicide phases, oxygen content, Ti residual layer etc. Here, for the thinner samples with much smaller grain size, the effect of grain boundaries, intergranular distance, the content and/or type of the intergranular region contribute significantly to the disorder as compared to that of the thicker samples. Furthermore, the substrate roughness [Fig. S4 in the SI] also becomes important for the thinner samples as that can induce disorder in the form of strain or probable weak links leading to PS.

In order to examine the effect of disorder on IVCs, we have studied more samples with reduced thickness and varying T_a. In Fig. 4, we present IVCs for two such samples TN5 and TN9 that are annealed at 820 °C & 780 °C, respectively. The samples from the 3 nm thickness batch. Here for sample TN5 with T_a = 820 °C in Fig. 4a, the intermediate resistive steps during the SC-to-NM transition become much more prominent and wide compared to that for 4 nm thick sample TN4 presented in Fig. 3b. Initially, IVC isotherms show almost single step transition for measurement temperature 2.3 K and below, whereas, for temperature above 2.3 K, the single step transition is converted into a multiple step transition from superconducting state to metallic state. Furthermore, compared to TN5, intermediate resistive steps get even more pronounced and broad for sample TN9, which was annealed at 780 °C as shown in the Fig. 4b. Unlike the sample TN8 annealed at 780 °C with thickness 4 nm presented in

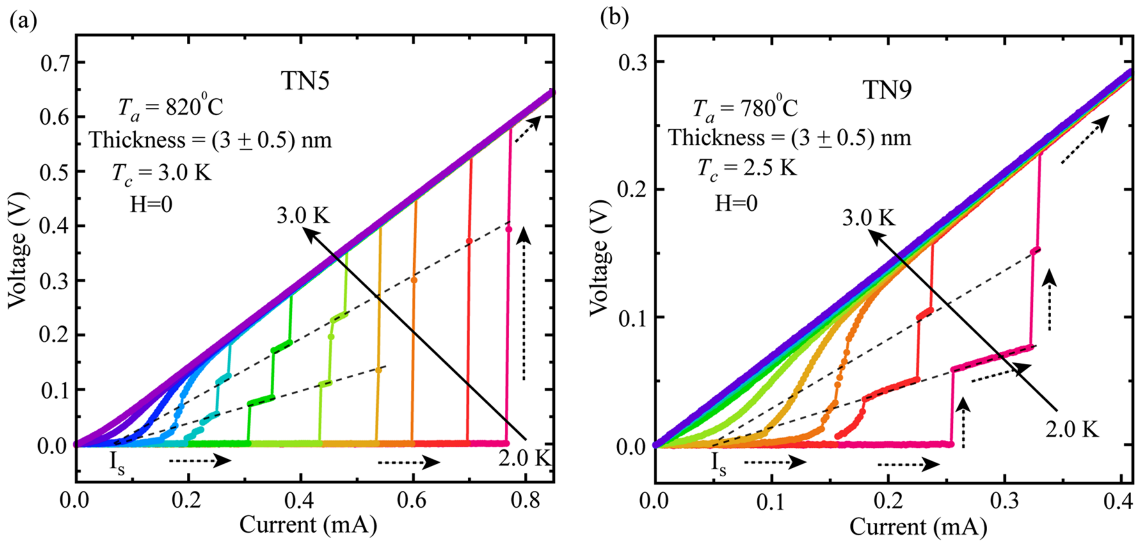

Figure 4. Isothermal IVCs measured on samples with reduced thickness. Zero-field IVC isotherms for (**a**) TN5 (~3 nm) annealed at 820 °C and (**b**) TN9 (~3 nm) annealed at 780 °C. Here, the samples TN5 and TN9 are of same thickness of about 3 nm. The dotted black arrows indicate the sweeping direction. The grey dashed lines indicate the convergence of the resistive states at the excess current I_s.

Fig. 3c, wide resistive states start to show up even at 2 K base temperature for TN9. These resistive steps are a signature of the formation of PSLs occurring due to the annihilation of vortex-antivortex pairs emerging from the edges of the films[37,43]. Therefore, both T_a & film thickness play crucial roles in altering the emergence of intermediate resistive steps in IVCs, however, the effect of film thickness is more prominent than that of T_a as the former introduces more disorder than the later.

In order to examine the effect of magnetic field on the IVCs of these disordered TiN thin film samples, we have selected two samples, TN4 and TN5, that were annealed at T_a = 820 °C but of thickness 4 nm and 3 nm, respectively. Here, IVCs were measured at varying magnetic field while keeping the measurement temperature unaltered. For sample TN4, the field dependent IVCs measured at 2.7 K are presented in Fig. 5a which shows single step transition from SC-to-NM state from 0–25 mT. With a further increase in the field up to 50 mT, an intermediate resistive step starts to appear in the course of the SC-to-NM transition instead of a single step transition. Here, the resistive step gets narrower in extent with increasing field and the same remains prominent up to 250 mT. With further increasing field, the intermediate step starts to diminish and the SC-NM transition gets smoother. Furthermore, the evolution of the intermediate resistive step with magnetic field has been displayed by the contour color plot in Fig. 5b with the support of the differential resistance (dV/dI) extracted from the measured field dependent IVCs. Considering the range of magnetic field within which the intermediate step appears, the contour plot in Fig. 5b is confined within 300 mT. Here, because of the single step transition, the differential resistance is maximum at 0–25 mT, whereas at higher fields, it gets reduced by the introduction of intermediate resistive steps that are indicated by the presence of multiple peaks at a particular field during the SC-NM transition. However, at 250 mT and above, presence of a single, and relatively stronger peak, in the dV/dI indicates the removal of intermediate steps by the external magnetic field. In Fig. 5b, the position corresponding to the peak of dV/dI at a particular magnetic field relates to the I_c which reduces as the field moves towards the higher side. As observed in Fig. 4, reduction in film thickness makes the intermediate resistive steps more prominent. In order to examine the effect of field on reduced film thickness, we have measured field dependent IVCs for the sample TN5 with thickness 3 nm at the measurement temperature 2.3 K and the same is exhibited in Fig. 5c. Here, the zero field IVC shows no intermediate steps but the steps start to emerge at 25 mT and remain prominent up to 175 mT. It is to be noted that with reduction in thickness from 4 to 3 nm, the number of intermediate steps increases indicating a greater number of transition segments in the SC-NM phase transition region. The same is evident by the appearance of multiple peaks in the concerned differential resistance dV/dI representation through the colour plot in Fig. 5d. From Fig. 5c,d, initially the intermediate steps get wider with increasing field up to about 100 mT and with further increasing field in the range between 125–175 mT, the wide steps start to break up into a greater number of steps. The splitting of the steps is clearly evident by the presence of multiple low-amplitude dV/dI peaks encircled by the dotted region in Fig. 5d. Furthermore, intermediate sharp resistive steps start to disappear at 200 mT and there is a gradual increase in voltage from superconducting to normal state with a very little variation in differential resistance.

Further, we have extracted the critical current (I_c) and retrapping current (I_r) from the IVCs at zero field for five representative samples TN4, TN5, TN8, TN9 and TN12. Already, we have presented the effect of T_a and film thickness on the IVCs of disordered TiN thin films in Figs. 3 and 4. Here, we show the influence of T_a and film thickness on the temperature dependent I_c & I_r. We have investigated the temperature dependence of I_c in the light of Ginzburg- Landau (GL) theory[32] and modified GL theory[44] whereas, the I_r has been explained by the existing hotspot model given by Skocpol, Beasley, and Tinkham (SBT)[38]. We have found that the theoretical GL

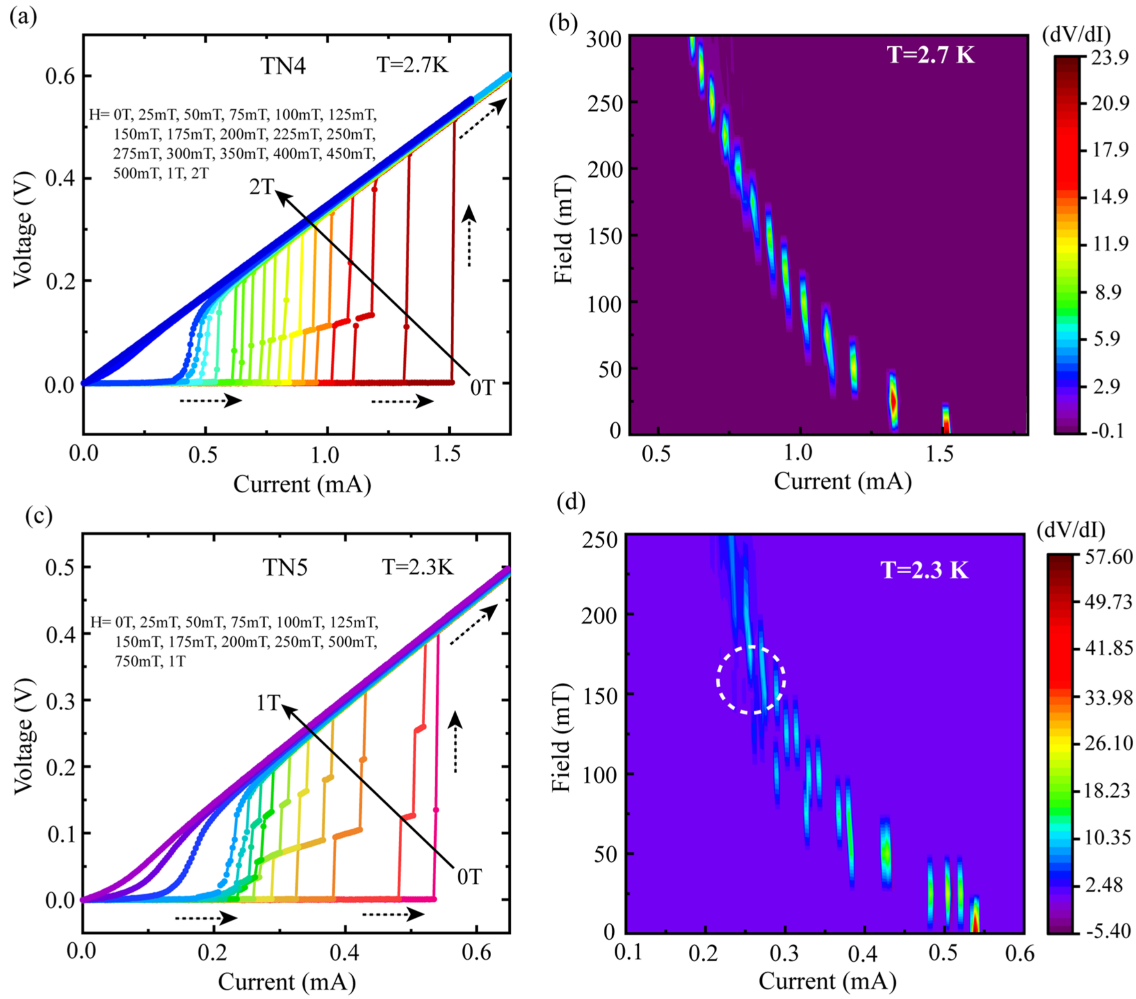

Figure 5. Magnetic field dependence of IVCs for samples TN4 (~ 4 nm) and TN5 (~ 3 nm) that are annealed at 820 °C. (**a**) Field-dependent IVCs for sample TN4 measured at fixed temperature 2.7 K and (**b**) corresponding dV/dI with respect to field & current in 3-D colour plot. (**c**) Variation of IVCs with magnetic field but at fixed temperature 2.3 K for sample TN5 and (**d**) the related dV/dI with respect to field & current in 3-D representation using contour colour plot. The Black solid arrows and dotted arrows in (**a**,**c**) indicate the increasing direction of applied magnetic field and the current sweeping direction, respectively.

equation $I_c \propto (1-t)^{s'}$; with $s' = 3/2$ is valid near the T_c to explain the temperature dependent I_c and it deviates at temperature far below the T_c ($T < 0.75T_c$) as shown by the blue dotted curves in Fig. 6a,b,d for samples TN4, TN8 and TN5, respectively. In order to fit entire range of measured temperature points, we have adopted the modified GL Eq[44], $I_c \propto (1-t^2)^s(1+t^2)^{1/2}$, where we use the exponent 's' as the free parameter to have the best fit to the experimental data. The red solid curves represent the best fits using the aforementioned modified GL equation for the samples presented in Fig. 6a,b,d with the exponent values 1.32, 1.35 and 1.70, respectively. The acquired exponent (s) values from the fitting are close to the theoretical value of exponent around 1.5[32]. However, the difference of about 0.03 in the exponent s, for the samples with same thickness of 4 nm (TN4 & TN8), is negligible compared to the difference of about 0.35 for the sample TN5 of 3 nm thickness with the samples having thickness of 4 nm (TN4 or TN8). Further, for samples TN12 [Fig. 6c] and TN9 [Fig. 6e], the measured temperature varies within $0.75T_c$ and T_c, and we obtain the best fits (the solid blue curves) using the GL equation. where the exponent s' is used as a free parameter. Here, the values for the exponent s' from the fits are 1.31 and 1.83 for TN12 and TN9, respectively. The exponent for the sample TN12 of 4 nm thickness is close to the theoretical value[32] and also is similar to the other 4 nm thick samples TN4 &TN8. However, the deviation in the exponent for the sample TN9 with thickness of 3 nm from the theoretical value is more and is on the higher side. Furthermore, the fits from two other 3 nm samples, TN5 & TN9, thickness have offered exponent values that are very close to each other. Therefore, it is evident from the above critical current analysis that the thickness, and hence, the disorder plays a significant role in controlling the temperature dependent I_c in wide disordered superconducting thin films. Here, we observed that the exponent values, as obtained from the fits for 4 nm thick samples (TN4, TN8, TN12) are of the same order and lower than the theoretical value and 3 nm thick samples (TN5&TN9) have exponent values much higher than the theoretical value of 1.5. The higher exponent is mainly due to the presence of higher level of disorder in thinner samples. Apart from I_c, we have

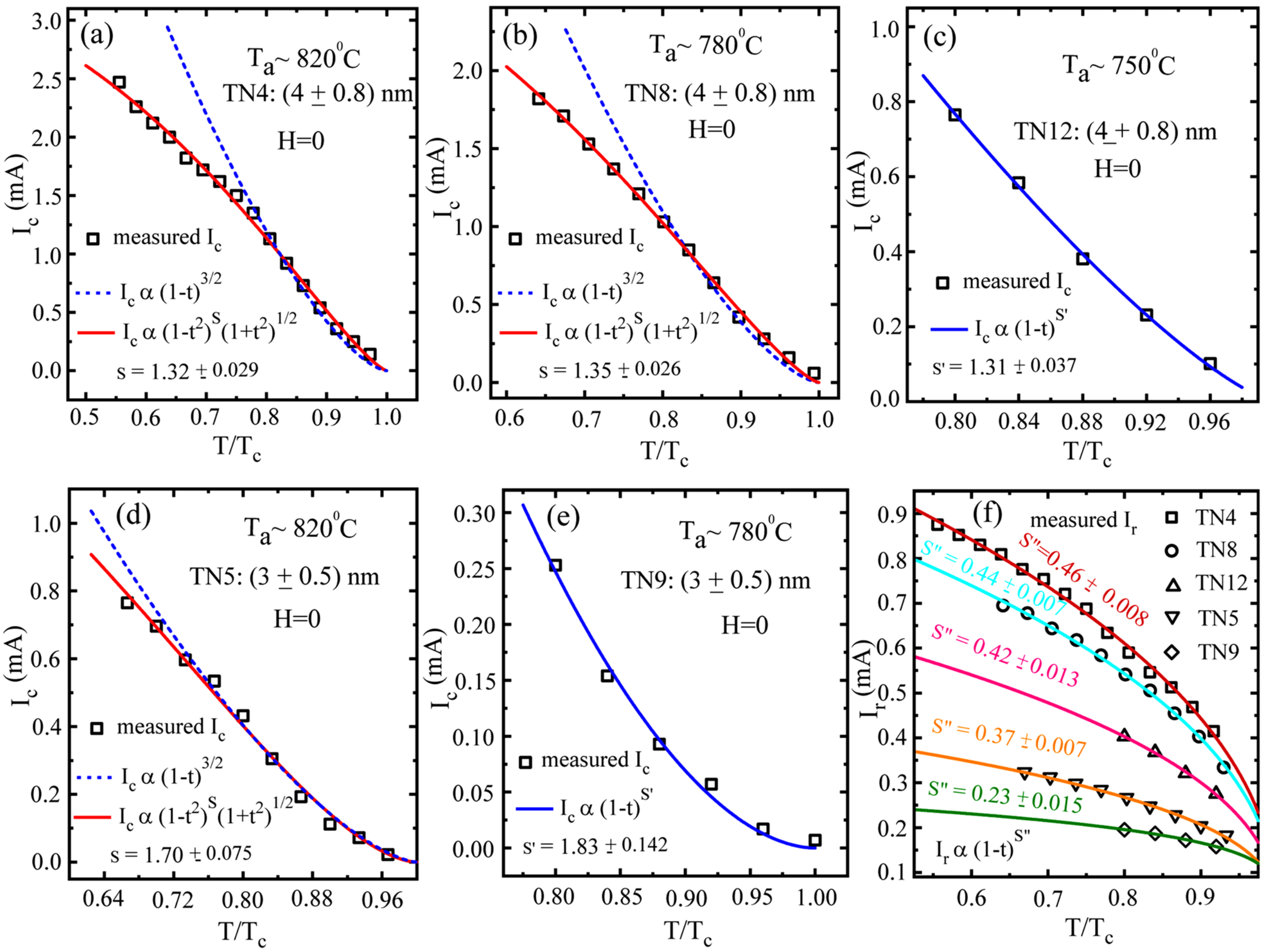

Figure 6. Temperature dependence of characteristic currents such as critical current (I_c) and retrapping current (I_r). Dependence of I_c on reduced temperature (T/T_c) for samples (**a**) TN4 annealed at 820 °C, (**b**)TN8 annealed at 780 °C, (**c**)TN12 annealed at 750 °C, (**d**)TN5 annealed at 820 °C and (**e**)TN9 annealed at 820 °C. The samples in the first row, (**a**–**c**), are having the same film thickness of about 4 nm, whereas, the samples presented in (**d**,**e**) are having thickness of about 3 nm. The blue dotted lines indicate the fitting on the experimental data points close to the T_c by using the Ginzburg–Landau (GL) eqn. $I_c \propto (1-t)^{3/2}$, where $t = T/\ T_c$. The red solid lines are the fits obtained by using the modified GL eqn. $I_c \propto (1-t^2)^s(1+t^2)^{1/2}$, fitted over the entire range of measured temperature. However, blue solid lines in (**c**,**e**) give the best fit by using the GL equation with a free exponent s′ instead of fixing it to 3/2 for samples TN9 & TN12 at temperature close to the T_c. (**f**) I_r related to all the five samples TN4, TN5, TN8, TN9 and TN12. For I_r, SBT model was used to fit the experimental data and the solid-colored lines represent the fitted curves by using eqn. $I_r \propto (1-t)^{s''}$.

measured the temperature dependent I_r for all the above five samples and the collection of those is presented in Fig. 6f. First, we observe that the amplitude of I_r reduces with the reduction in T_a for the samples having same thickness. Similarly, reduction in thickness also reduces the I_r for samples annealed at same T_a. Therefore, I_c and I_r follow the similar trend as that of T_c with the variations in thickness and T_a. In the present case due to hysteretic IVCs, I_c and I_r are different and this is mainly due to the Joule heating in the resistive state[38CitationID="CR39">39]. Therefore, we have used the SBT hotspot model using equation, $I_r \propto (1-t)^{s''}$, to fit the retrapping current. Here, $s'' = 1/2$ is the theoretical value. The best fitted colored curves, using the exponent s'' as a free parameter, are presented in Fig. 6f for individual samples. The exponent for the samples TN4 ($s'' = 0.46$), TN8 ($s'' = 0.44$) & TN12 ($s'' = 0.42$) are close to the theoretical value of 0.5, whereas, there is a small deviation from the theoretical value for the sample TN5 ($s'' = 0.37$) and a further deviation appears for TN9 ($s'' = 0.23$). The deviation in exponent values from the theoretical value increases with decreasing T_a and reduction in thickness indicating the influence of disorder on the mechanism of depairing current limit. Here depairing current refers to the maximum dissipationless current carried by a superconductor. Finally, the influence of T_a and film thickness on the I_c and I_r is reflected by the various exponent values used to explain and understand the experimental results by using the existing models[32,38,44].From the temperature dependent critical current analysis, the effect of T_a on the exponent remains almost invariant ($s \sim 1.3$), whereas, the effect of thickness plays a significant role in tuning the exponent values that shoot up with decreasing film thickness. Interestingly, the resistive steps appearing in the IVCs presented in Figs. 3 & 4, get more prominent and wider for reduced thickness rather than T_a. Finally, the reduced film thickness leads to suppression of T_c & I_c, the appearance of PSLs in IVCs, and the deviation of

Samples	T_a, (°C) ± 10 °C	d, (nm)	T_C, (K)	ΔT, (K)	ξ(0), (nm)	R_n^{300K}, (Ω)	RRR = (R_n^{300K}/R_n^{6K})	ρ_n (6 K), (μ-Ωcm)	Intermediate steps in IVCs @ zero-field
TN1	820	20 ± 2	4.8	0.2	–	47	1.70	34.5	–
TN2	820	12 ± 1	4.76	0.2	9.5	140	1.61	65	–
TN3	820	8 ± 1	4.4	0.25	–	214	1.39	77	–
TN4	820	4 ± 0.8	3.6	0.23	8.7	408	1.24	82	Majorly single step transition
TN5	820	3 ± 0.5	3.0	0.32	7.94	879	1.14	135	Multiple step transition
TN6	820	2 ± 0.5	–	–	–	25,742	0.70	4588	–
TN7	780	12 ± 1	4.38	0.18	10.8	98	1.54	47	Single step transition
TN8	780	4 ± 0.8	3.12	0.26	9.2	370	1.21	75	Multiple step transition
TN9	780	3 ± 0.5	2.5	0.28	9.0	808	1.10	127	Multiple step transition
TN10	780	2 ± 0.5	–	–	–	2650	0.98	338	–
TN11	750	12 ± 1	3.52	0.3	9.6	83	1.38	45	Single step transition
TN12	750	4 ± 0.8	2.5	0.27	10	383	1.18	81	Multiple step transition
TN13	750	3 ± 0.5	2.4	0.29	–	851	1.10	133	–
TN14	700	12 ± 1	2.0	0.25	–	99	1.24	60	–
TN15	700	4 ± 0.8	–	–	–	473	1.08	109	–
TN16	650	12 ± 1	–	–	–	200	1.10	136	–

Table 1. Superconducting parameters obtained for TiN thin films fabricated by using the substrate mediated nitridation technique.

the temperature dependent critical current from its theoretical value. Therefore, the enhanced level of disorder due to the reduction in film thickness plays a very important role in monitoring the superconducting properties and the overall SC-NM phase transition.

Conclusion

In conclusion, we have fabricated disordered superconducting TiN thin films by establishing an unconventional but robust, nitridation method which involves high temperature annealing of Ti thin films deposited on Si_3N_4/Si substrates. The annealing process leads to the decomposition of Si_3N_4 into N and Si atoms that form majority TiN and minority $TiSi_2$ phases by reacting with Ti[18]. Generally, disorder is present in pure thin films and here the presence of $TiSi_2$ and excess Si can further enhance the level of disorder. The best obtained T_c among the measured samples is ~ 4.8 K for film thickness of about 12 nm and above. As expected, T_a plays a very important role in tuning the T_c. We also show that the T_c and R_n depend strongly on the film thickness. Furthermore, the IVCs for ultrathin (≤ 4 nm) samples feature staircase-like steps indicating the appearance of PSLs that evolve more prominently with the reduction in thickness and by external magnetic fields. Finally, the T_c achieved by using this technique is comparable to the best reported values in the literature (Table S1). Other superconducting parameters are summarized in Table 1. Furthermore, the T_c, PSLs and the temperature dependent critical current vary in a similar fashion on the growth parameters like T_a and the thickness.

Methods

Material synthesis through a novel technique. We used undoped intrinsic Si (100) substrate covered with 80 nm Si_3N_4 dielectric spacer layer, grown by low pressure chemical vapor deposition (LPCVD), as the substrate for the growth of TiN films. The substrates were cleaned by using the standard cleaning process involving sonication in acetone and isopropanol bath for 15 min each, followed by oxygen plasma cleaning of 10 min. Thereafter cleaned samples were loaded into the sputtering unit and transferred to ultra-high vacuum (UHV) chamber where they were pre-heated at about 820 °C for 30 min under very high vacuum conditions ($p \sim 5 \times 10^{-8}$ Torr) in order to remove any adsorbed or trapped molecules/residue on the surface of the substrate. After performing all the cleaning process, cleaned Si_3N_4/Si substrate was cooled down to room temperature and transferred to the sputtering chamber through load lock without breaking the vacuum. A thin layer of Ti was then deposited on the substrate by dc magnetron sputtering of Ti (99.995% purity) in the presence of high purity Ar (99.9999%) gas. Sputtering of Ti was performed with a base pressure less than 1.5×10^{-7} Torr. Finally, the sputtered sample was transferred again into the UHV chamber for post-sputtering annealing. Ti films on Si_3N_4/Si (100) were annealed at different annealing temperatures (~ 820 °C, ~ 780 °C, ~ 750 °C, ~ 700 °C and ~ 650 °C) for 2 h at a pressure less than 5×10^{-8} Torr. The thickness values for the films are determined by the optimized rate and thickness measurements on various samples prepared with same deposition time. The average value obtained from the thickness measurements is assigned to the thickness and the errors represent the range of variations on the measured values. Here, variation in annealing temperature is within ± 10 °C. During the annealing process, Si_3N_4 decomposes into Si and N atoms and due to high affinity of titanium towards both nitrogen and silicon, stable stoichiometric cubic titanium nitride (TiN) forms as a majority phase along with the minority phases such a titanium silicide ($TiSi_2$) and elemental silicon (Si). Here, temperature plays an important role to control the chemical kinetics happening during the chemical reaction because phenomena like decomposition and diffusion are very much sensitive to temperature. Therefore, concentration of majority and minority phases varies with the annealing temperatures (T_a) such as for $T_a > 780$ °C, majority phase is accompanied by elemental Si rather than silicide phase, whereas for $T_a \leq 780$ °C, it is accompanied by silicide phase. The concentration of silicide phase is maximum for $T_a \sim 780$ °C and the same gets reduced with the decrease in T_a.

For structural characterization we fabricated thin films on substrates with an area of 5 mm × 5 mm. For the transport measurements, we have patterned the thin films into Hall bar geometry by using shadow mask made of stainless steel. We have used a complimentary separate mask to make the contact leads for voltage and currents probes. The device geometry for a representative device is shown in the inset of Fig. 1a. The contact leads were made of Au (~ 50 nm)/Ti (~ 5 nm) deposited by dc magnetron sputtering.

Structural characterizations. Photoelectron Spectroscopic (XPS) measurements were performed in UHV based Multiprobe Surface Analysis System (Thermo Scientific Nexsa) operating at a base pressure of 1.5×10^{-7} Pa. A monochromatic Al-Kα radiation source (1486.7 eV) was employed with radiation spot size of 400 μm for the excitation. To enhance the sampling depth and minimize the contribution of native oxides & contaminants, in-situ sputtering via energetic Ar^+ ions (at 500 eV) was performed for about 2 min. The depth profile scan was taken in "snapshot mode" in order to reduce the data acquisition time at the expense of spectra resolution. The adventitious carbon C–C bond at 284.8 eV was used for binding energy correction.

Morphological characterizations. The morphological characterizations of the samples were performed by using scanning electron microscope (Gemini SEM 500 ZEISS) and atomic force microscope (AFM) from BRUKER, Dimension ICON, in tapping mode.

Low temperature transport measurements. Transport measurements were carried out using a 16 T/2 K Physical Properties Measurement System (PPMS) of Quantum Design, USA at UGC-DAE CSR Indore.

Data availability

The data that represent the results in this paper and the data that support the findings of this study are available from the corresponding author upon reasonable request.

Received: 5 January 2021; Accepted: 19 March 2021
Published online: 12 April 2021

References

1. Dubi, Y., Meir, Y. & Avishai, Y. Nature of the superconductor–insulator transition in disordered superconductors. *Nature* **449**, 876–880 (2007).
2. Sacépé, B. *et al.* Disorder-induced inhomogeneities of the superconducting state close to the superconductor–insulator transition. *Phys. Rev. Lett.* **101**, 157006 (2008).
3. Swanson, M., Loh, Y. L., Randeria, M. & Trivedi, N. Dynamical conductivity across the disorder-tuned superconductor-insulator transition. *Phys. Rev. X* **4**, 021007 (2014).
4. Shi, X., Lin, P. V., Sasagawa, T., Dobrosavljević, V. & Popović, D. Two-stage magnetic-field-tuned superconductor–insulator transition in underdoped La2−xSrxCuO4. *Nat. Phys.* **10**, 437–443 (2014).
5. Astafiev, O. V. *et al.* Coherent quantum phase slip. *Nature* **484**, 355–358 (2012).
6. Mooij, J. E. & Nazarov, Y. V. Superconducting nanowires as quantum phase-slip junctions. *Nat. Phys.* **2**, 169–172 (2006).
7. Berdiyorov, G. R., Milošević, M. V. & Peeters, F. M. Kinematic vortex-antivortex lines in strongly driven superconducting stripes. *Phys. Rev. B* **79**, 184506 (2009).
8. Sivakov, A. G. *et al.* Josephson behavior of phase-slip lines in wide superconducting strips. *Phys. Rev. Lett.* **91**, 267001 (2003).
9. Kimmel, G., Glatz, A. & Aranson, I. S. Phase slips in superconducting weak links. *Phys. Rev. B* **95**, 014518 (2017).
10. Michotte, S., Mátéfi-Tempfli, S., Piraux, L., Vodolazov, D. Y. & Peeters, F. M. Condition for the occurrence of phase slip centers in superconducting nanowires under applied current or voltage. *Phys. Rev. B* **69**, 094512 (2004).
11. Bawa, A., Jha, R. & Sahoo, S. Tailoring phase slip events through magnetic doping in superconductor-ferromagnet composite films. *Sci. Rep.* **5**, 13459 (2015).
12. Bawa, A., Gupta, A., Singh, S., Awana, V. P. S. & Sahoo, S. Ultrasensitive interplay between ferromagnetism and superconductivity in NbGd composite thin films. *Sci. Rep.* **6**, 18689 (2016).
13. Adami, O. A. *et al.* Onset, evolution, and magnetic braking of vortex lattice instabilities in nanostructured superconducting films. *Phys. Rev. B* **92**, 134506 (2015).
14. Baturina, T. I., Mironov, A. Y., Vinokur, V. M., Baklanov, M. R. & Strunk, C. Localized superconductivity in the quantum-critical region of the disorder-driven superconductor-insulator transition in TiN thin films. *Phys. Rev. Lett.* **99**, 257003 (2007).
15. Vinokur, V. M. *et al.* Superinsulator and quantum synchronization. *Nature* **452**, 613–615 (2008).
16. Sacépé, B. *et al.* Localization of preformed Cooper pairs in disordered superconductors. *Nat. Phys.* **7**, 239–244 (2011).
17. Sacépé, B. *et al.* Pseudogap in a thin film of a conventional superconductor. *Nat. Commun.* **1**, 140 (2010).
18. Yadav, S. & Sahoo, S. Interface study of thermally driven chemical kinetics involved in Ti/Si3N4 based metal-substrate assembly by X-ray photoelectron spectroscopy. *Appl. Surf. Sci.* **541**, 148465 (2021).
19. Yadav, S. *et al.* Substrate mediated synthesis of Ti–Si–N nano-and-micro structures for optoelectronic applications. *Adv. Eng. Mater.* **21**, 1900061 (2019).
20. Gajar, B. *et al.* Substrate mediated nitridation of niobium into superconducting Nb2N thin films for phase slip study. *Sci. Rep.* **9**, 8811 (2019).
21. Kardakova, A. *et al.* The electron–phonon relaxation time in thin superconducting titanium nitride films. *Appl. Phys. Lett.* **103**, 252602 (2013).
22. Sun, R., Makise, K., Qiu, W., Terai, H. & Wang, Z. Fabrication of (200)-oriented TiN films on Si (100) substrates by DC magnetron sputtering. *IEEE Trans. Appl. Supercond.* **25**, 1–4 (2015).

23. Vissers, M. R. *et al.* Characterization and in-situ monitoring of sub-stoichiometric adjustable superconducting critical temperature titanium nitride growth. *Thin Solid Films* **548**, 485–488 (2013).
24. Leduc, H. G. *et al.* Titanium nitride films for ultrasensitive microresonator detectors. *Appl. Phys. Lett.* **97**, 102509 (2010).
25. Jaim, H. M. I. *et al.* Superconducting TiN films sputtered over a large range of substrate DC bias. *IEEE Trans. Appl. Supercond.* **25**, 1–5 (2015).
26. Ohya, S. *et al.* Room temperature deposition of sputtered TiN films for superconducting coplanar waveguide resonators. *Supercond. Sci. Technol.* **27**, 015009 (2013).
27. Shearrow, A. *et al.* Atomic layer deposition of titanium nitride for quantum circuits. *Appl. Phys. Lett.* **113**, 212601 (2018).
28. Pracht, U. S. *et al.* Direct observation of the superconducting gap in a thin film of titanium nitride using terahertz spectroscopy. *Phys. Rev. B* **86**, 184503 (2012).
29. Spengler, W., Kaiser, R., Christensen, A. N. & Müller-Vogt, G. Raman scattering, superconductivity, and phonon density of states of stoichiometric and nonstoichiometric TiN. *Phys. Rev. B* **17**, 1095–1101 (1978).
30. Krockenberger, Y., Karimoto, S.-I., Yamamoto, H. & Semba, K. Coherent growth of superconducting TiN thin films by plasma enhanced molecular beam epitaxy. *J. Appl. Phys.* **112**, 083920 (2012).
31. Torgovkin, A. *et al.* High quality superconducting titanium nitride thin film growth using infrared pulsed laser deposition. *Supercond. Sci. Technol.* **31**, 055017 (2018).
32. Kupryanov, M. Y. & Lukichev, V. F. Temperature dependence of pair-breaking current in superconductors. *Sov. J. Low Temp. Phys.* **6**, 210 (1980).
33. Kemper, M. J. H. & Oosting, P. H. Crystallization and resistivity of amorphous titanium silicide films deposited by coevaporation. *J. Appl. Phys.* **53**, 6214–6219 (1982).
34. Patsalas, P., Charitidis, C., Logothetidis, S., Dimitriadis, C. A. & Valassiades, O. Combined electrical and mechanical properties of titanium nitride thin films as metallization materials. *J. Appl. Phys.* **86**, 5296–5298 (1999).
35. Delacour, C., Pannetier, B., Villegier, J.-C. & Bouchiat, V. Quantum and thermal phase slips in superconducting niobium nitride (NbN) ultrathin crystalline nanowire: Application to single photon detection. *Nano Lett.* **12**, 3501–3506 (2012).
36. Jelila, F. S. *et al.* Time of Nucleation Of Phase-Slip Centers in YBa2Cu3O7 superconducting bridges. *Phys. Rev. Lett.* **81**, 1933–1936 (1998).
37. Berdiyorov, G. *et al.* Dynamics of current-driven phase-slip centers in superconducting strips. *Phys. Rev. B* **90**, 054506 (2014).
38. Skocpol, W. J., Beasley, M. R. & Tinkham, M. Self-heating hotspots in superconducting thin-film microbridges. *J. Appl. Phys.* **45**, 4054–4066 (1974).
39. Skocpol, W. J. & Tinkham, M. Fluctuations near superconducting phase transitions. *Rep. Prog. Phys.* **38**, 1049–1097 (1975).
40. Burdastyh, M. V. *et al.* Superconductor–insulator transition in NbTiN films. *JETP Lett.* **106**, 749–753 (2017).
41. Postolova, S. V., Mironov, A. Y., Baklanov, M. R., Vinokur, V. M. & Baturina, T. I. Reentrant resistive behavior and dimensional crossover in disordered superconducting TiN films. *Sci. Rep.* **7**, 1718 (2017).
42. Jang, H.-B., Lim, J. S. & Yang, C.-H. Film-thickness-driven superconductor to insulator transition in cuprate superconductors. *Sci. Rep.* **10**, 3236 (2020).
43. Vodolazov, D. Y. & Peeters, F. M. Rearrangement of the vortex lattice due to instabilities of vortex flow. *Phys. Rev. B* **76**, 014521 (2007).
44. Scharnhorst, P. Critical currents in superconducting tin and indium. *Phys. Rev. B* **1**, 4295–4304 (1970).

Acknowledgements

The authors highly acknowledge UGC-DAE CSR, Indore, India for carrying out the low temperature measurements in PPMS. We are thankful to the central facilities at IIT, Mandi, India for carrying out the XPS, SEM and AFM characterizations. We highly acknowledge Mr. Kumar Palit from IIT, Mandi, for his prompt response in carrying out the SEM and AFM characterizations within a very short period of time. We express our sincere thanks to Dr. Sudhir Husale for his support in SEM characterization. We are thankful to Mr. M. B. Chhetri, Mr. Bikash Gajar & Ms. Deepika Sawle for their assistance in the lab. S.Y. acknowledges the Senior Research fellowship (SRF) from UGC. Authors acknowledge the financial support for establishing the dilution refrigerator facility at CSIR-NPL from the Department of Science and Technology (DST), Govt. of India, under the project, SR/52/pu-0003/2010(G). This work was supported by CSIR network project 'AQuaRIUS' (Project No. PSC 0110) and is carried out under the mission mode project "Quantum Current Metrology".

Author contributions

S.Y. and S.S. fabricated the devices. S.Y., V.K., M.P.S., V.G. and R.P.A. carried out the low temperature transport measurements. S.Y. and S.S. analyzed the data and S.Y. wrote the manuscript. S.S. planned, designed and supervised the project. All the authors read and reviewed the manuscript.

Competing interests

The authors declare no competing interests.

Additional information

Supplementary Information The online version contains supplementary material available at https://doi.org/10.1038/s41598-021-86819-6.

Correspondence and requests for materials should be addressed to S.S.

Reprints and permissions information is available at www.nature.com/reprints.

Publisher's note Springer Nature remains neutral with regard to jurisdictional claims in published maps and institutional affiliations.